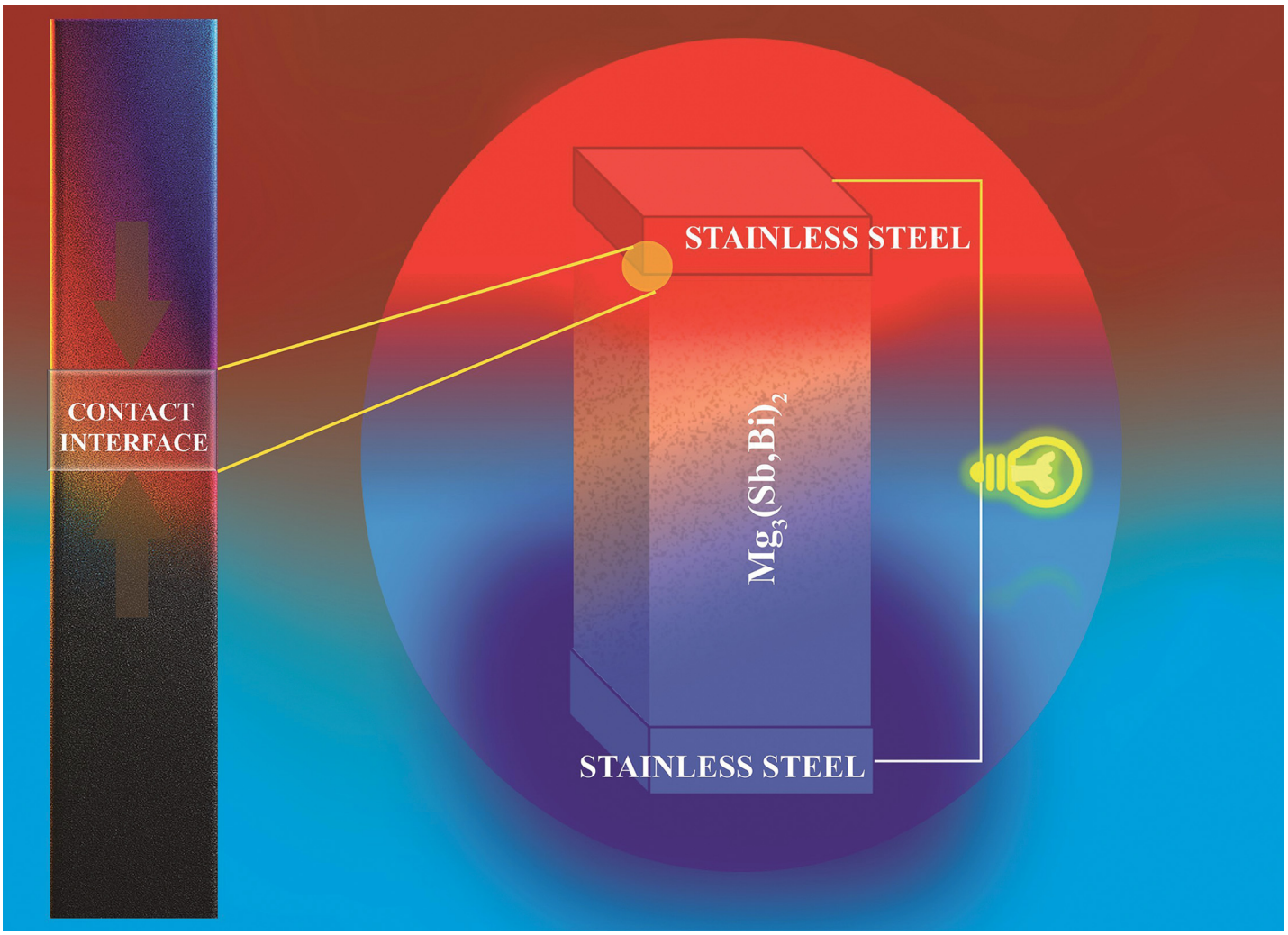

Showing research from Thermoelectric Materials Group, Research Center for Materials Nanoarchitectonics (MANA), National Institute for Materials Science (NIMS), Japan.

Process optimization of contact interface layer for maximizing the performance of $Mg_3(Sb,Bi)_2$ based thermoelectric compounds

This work demonstrates the reduction of specific contact resistivity (ρc) through the optimization of sintering temperatures, leading to a maximum conversion efficiency (η_{max}) of 9.3% at ΔT = 380 K for $SS_f/Mg_3Sb_{1.5}Bi_{0.5}/SS_f$ thermoelectric (TE) single leg, emphasizing the potential of stainless-steel foil (SS_f) interface layer for thermoelectric applications.

Image reproduced by permission of Takao Mori from *J. Mater. Chem. C*, 2025, **13**, 10567.

As featured in:

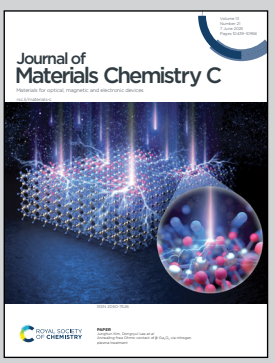

See Raju Chetty, Takao Mori *et al.*, *J. Mater. Chem. C*, 2025, **13**, 10567.

ROYAL SOCIETY OF CHEMISTRY

rsc.li/materials-c

Registered charity number: 207890

Journal of Materials Chemistry C

ROYAL SOCIETY OF CHEMISTRY

PAPER

View Article Online
View Journal | View Issue

Cite this: J. Mater. Chem. C, 2025, 13, 10567

Process optimization of contact interface layer for maximizing the performance of $Mg_3(Sb,Bi)_2$ based thermoelectric compounds†

Muhammad Fasih Aamir,[ab] Raju Chetty,*[a] Jayachandran Babu[a] and Takao Mori*[ab]

Received 26th February 2025,
Accepted 26th April 2025

DOI: 10.1039/d5tc00851d

rsc.li/materials-c

$Mg_3(Sb,Bi)_2$ based compounds exhibit promising thermoelectric (TE) performance within the 300–700 K range, making them suitable for mid-temperature applications; yet achieving optimal electrical contact between the TE material and the contact material is crucial. One-step sintering has emerged as a widely used technique for establishing these contacts in $Mg_3(Sb,Bi)_2$ compounds, though variations in process parameters can impact contact quality and, consequently TE conversion efficiency. Therefore, this study explores the optimization of $Mg_3(Sb,Bi)_2$ compounds using spark plasma sintering with stainless steel (SS) 304 contacts at three different temperatures of 973 K, 1023 K, and 1073 K. By increasing the sintering temperature from 973 K to 1073 K, a significant reduction in the specific contact resistivity (ρ_c) by ~60% is realized, without compromising TE properties. Furthermore, it was found that replacing SS powder (SS_p) with SS foil (SS_f) could lead to more uniform and dense layers, achieving a lower specific ρ_c value of 8.2 μΩ cm^2 at the interface. A maximum conversion efficiency (η_{max}) of ~9.3% was obtained at a temperature difference (ΔT) of ~380 K for $SS_f/Mg_3(Sb,Bi)_2/SS_f$ sintered at 1073 K. Moreover, thermal aging for 30 days at 673 K confirms the robustness of $SS_f/Mg_3(Sb,Bi)_2/SS_f$ contacts with negligible degradation of TE properties and conversion efficiency of the TE single leg.

1. Introduction

Approximately 66% of the energy used in factories, power plants, and other appliances is lost as heat.[1] Thermoelectric (TE) technology is a promising solution to convert this waste heat into electrical power while reducing the environmental impact of CO_2 emission.[2] TE devices offer benefits like zero pollution, silent operation, no moving parts, precise temperature control, and long service life, making them suitable for various applications, including energy harvesting, refrigeration, and space exploration.[3–7]

Conventional TE devices mostly comprise n-type and p-type compounds, connected electrically in series and thermally in parallel *via* metal electrodes.[8] When a temperature difference is applied across the TE device, a thermovoltage (V) is generated due to the Seebeck effect.[9] A connected electrical load causes current flow (I) through the TE device, which generates the useful electric power ($P = V \times I$).[10] The power conversion efficiency (η) of TE devices is defined as $\eta = \frac{P}{Q_{in}}$, where Q_{in} is the heat flow on the hot side.[11] The relationship between maximum conversion efficiency and TE material properties follows the equation[12,13]

$$\eta_{max} = \frac{\Delta T}{T_H} \frac{\sqrt{1+ZT}-1}{\sqrt{1+ZT}+\frac{T_C}{T_H}} \quad (1)$$

where ZT is the dimensionless figure of merit of TE materials, defined as $ZT = \frac{S^2\sigma T}{\kappa}$, where S = Seebeck coefficient, σ = electrical conductivity, κ = total thermal conductivity, and T = absolute temperature.[14] Several TE materials such as Bi_2Te_3,[15–19] PbTe,[20–27] SiGe,[28–31] skutterudites[32–38] and half-Heuslers[39–43] have shown promising ZT values.[44,45] To realize high conversion efficiencies in TE devices, the electrical contacts at various interfaces play a crucial role despite the high material ZT values.[46] Xiong *et al.* suggested a relationship between the

[a] Research Center for Materials Nanoarchitectonics (MANA), National Institute for Materials Science (NIMS), 1-1 Namiki, Tsukuba 305-0044, Japan. E-mail: chetty.raju@nims.go.jp, mori.takao@nims.go.jp
[b] Graduate School of Science and Technology, University of Tsukuba, 1-1-1 Tennodai, Tsukuba, Ibaraki 305-8577, Japan

† Electronic supplementary information (ESI) available. See DOI: https://doi.org/10.1039/d5tc00851d

TE material ZT and the device ZT (ZT_D) according to the equation

$$ZT_D = \frac{L}{L + 2\rho_c\sigma} ZT \quad (2)$$

where L, σ and ρ_c are the length, electrical conductivity of the TE compound, and the specific contact resistivity across the TE compound/electrode interface.[47] Typically, the TE compound/electrode contact should exhibit ohmic behavior with a contact resistivity of $\rho_c \leq 10^{-10}$ Ω m^2 to achieve high ZT_D values and conversion efficiency.[48]

$Mg_3(Sb,Bi)_2$ compounds have recently emerged as promising TE materials with good ZT at mid-range temperatures.[49–56] The high ZT values in these compounds have led to the realization of high TE conversion efficiencies.[57–61] However, the conversion efficiencies are still lower than expected due to the higher contact resistivities at the interfaces.[57] Therefore, several studies have been conducted to reduce the ρ_c by interfacial engineering of contact layers.[48,51,53,55] Pure metals like Ti,[61] Fe,[59] Ni,[62] and Nb[63] are explored as contact interface layers for the $Mg_3(Sb,Bi)_2$ compounds. Amongst them, Fe is the mostly used contact layer for $Mg_3(Sb,Bi)_2$. However, various reports show an inconsistency in the ρ_c that varies between 2.5×10^{-10} and 43.6×10^{-10} Ω m^2.[48,64–70] Not to mention that the incompatibility of Fe with the solder and the high specific contact resistivity (60 μΩ cm^2) at various interfaces after module operation is problematic.[65] While the ρ_c of 9.7 μΩ cm^2 was observed in the case of Nb/$Mg_3(Sb,Bi)_2$, which increased up to 26 μΩ cm^2 after module operation at 773 K for 360 h.[63] In case of the Ni contact interface layer, the ρ_c (18.56 μΩ cm^2) was also increased by 700% after aging at 673 K.[71] Apart from the above, metal alloys such as CuNi,[60] Mg_2Ni,[72] NiFe,[73] FeMgCrTiMn,[74] Fe_7Mg_2Cr & Fe_7Mg_2Ti,[48] stainless steel (SS304),[68] $Mg_{3.4}Sb_3Ni$[71] and Mg_2Cu[75] were also employed as contact layers to lower the ρ_c. In addition to the lowering of ρ_c, developing a thermally stable contact interface layer is crucial to realizing long-term TE device operation without deteriorating the conversion efficiency.

In this study, we focused on optimizing the fabrication process by varying the sintering temperature to lower the ρ_c and realize high conversion efficiency. Here we selected stainless steel 304 (SS) as a contact interface layer for the n-type $Mg_3(Sb,Bi)_2$ compound and fabricated *via* one-step sintering at different temperatures from 973 K to 1073 K. A significant reduction in ρ_c occurred from 19.7 μΩ cm^2 to 7.9 μΩ cm^2 by increasing the sintering temperature from 973 K to 1073 K. This is mainly attributed to strong adhesion between the SS and $Mg_3(Sb,Bi)_2$ at a higher sintering temperature. Furthermore, replacing SS powder (SS_p) with SS foil (SS_f) led to more uniform and dense interface layers. Consequently, a maximum conversion efficiency (η_{max}) of 9.3% is achieved at a temperature difference of 380 K. The long-term thermal stability of the $SS_f/Mg_3(Sb,Bi)_2/SS_f$ TE single leg was tested under isothermal (673 K) aging for 30 days, revealing a negligible diffusion between the SS_f and $Mg_3(Sb,Bi)_2$. As a result, no significant variation in the η_{max} value was found, confirming the good stability of SS_f as the contact interface layer for the $Mg_3(Sb,Bi)_2$ compounds.

2. Experimental techniques

2.1. Preparation of $Mg_3(Sb,Bi)_2$ TE materials and contacting

Ball milling (Sample Prep 8000, SPEX) was used to prepare the $Mg_{3.2}Sb_{1.5}Bi_{0.49}Te_{0.01}Cu_{0.01}$ bulk material (abbreviated as '$Mg_3Sb_{1.5}Bi_{0.5}$'). Ball-milled powders were loaded inside a graphite die of 10 mm in inner diameter and compacted using a spark plasma sintering (SPS-1080 System, SPS SYNTEX INC).

The single TE legs were fabricated by sandwiching the ball-milled $Mg_3Sb_{1.5}Bi_{0.5}$ powder between the layers of stainless steel 304 (SS) foils/powders. One-step sintering was carried out with SPS at different sintering temperatures (973 K, 1023 K, and 1073 K) under 60 MPa uniaxial pressure for 5 minutes. The prepared samples were diced into cuboid shapes using a wire saw. Mechanical polishing was done for the samples prepared for microstructural evaluation. For thermal stability studies, the samples were placed inside a sealed quartz ampoule and isothermally aged for 7, 15, and 30 days at 673 K.

Characterization

The phase purity of sintered pellets was characterized *via* X-ray diffraction (MiniFlex600, Rigaku Corporation). Microstructure analysis was carried out using a scanning electron microscope equipped with an EDX detector (SU8000, Hitachi High-Technologies/Bruker).

An approximately 3 mm × 3 mm × 9 mm cuboid sample was prepared for the combined Seebeck coefficient (S) and electrical conductivity (σ) measurements (ZEM-3, Advance Riko) and a 10 mm diameter cylindrical sample with 2 mm thickness for thermal diffusivity (λ) measurements (LFA 467, Netzsch). Thermal conductivity (κ) was estimated from the relation $\kappa = dC_p\lambda$ where 'd' is the mass density of the sample measured using the Archimedes technique and 'C_p' is the specific heat at constant pressure calculated from the Dulong–Petit limit.

Cuboid-shaped samples of approximately 3 × 3 × 5 mm^3 in volume were subjected to a resistance profiler to check the specific contact resistivity (ρ_c) which was obtained by measuring the contact resistance jump (ΔR) at the interfaces using the equation, $\rho_c = \Delta R \times A$, where '$A$' is the cross-sectional area. The power generation characteristics of the $SS/Mg_3Sb_{1.5}Bi_{0.5}/SS$ sample were measured using Mini PEM (Advance Riko).

3. Results and discussion

3.1. XRD and TE properties of $Mg_3Sb_{1.5}Bi_{0.5}$

The XRD patterns of $Mg_3Sb_{1.5}Bi_{0.5}$ pellets sintered at temperatures between 973 K and 1073 K are displayed in Fig. 1a. The diffraction peaks align with those of the $Mg_3Sb_{1.5}Bi_{0.5}$ phase, with no secondary phases for all the samples. XRD analysis reveals that all the sintered pellets exhibit a single phase.

Fig. 1b shows the temperature-dependent electrical conductivity (σ) of the $Mg_3Sb_{1.5}Bi_{0.5}$ pellets sintered between 973 K and

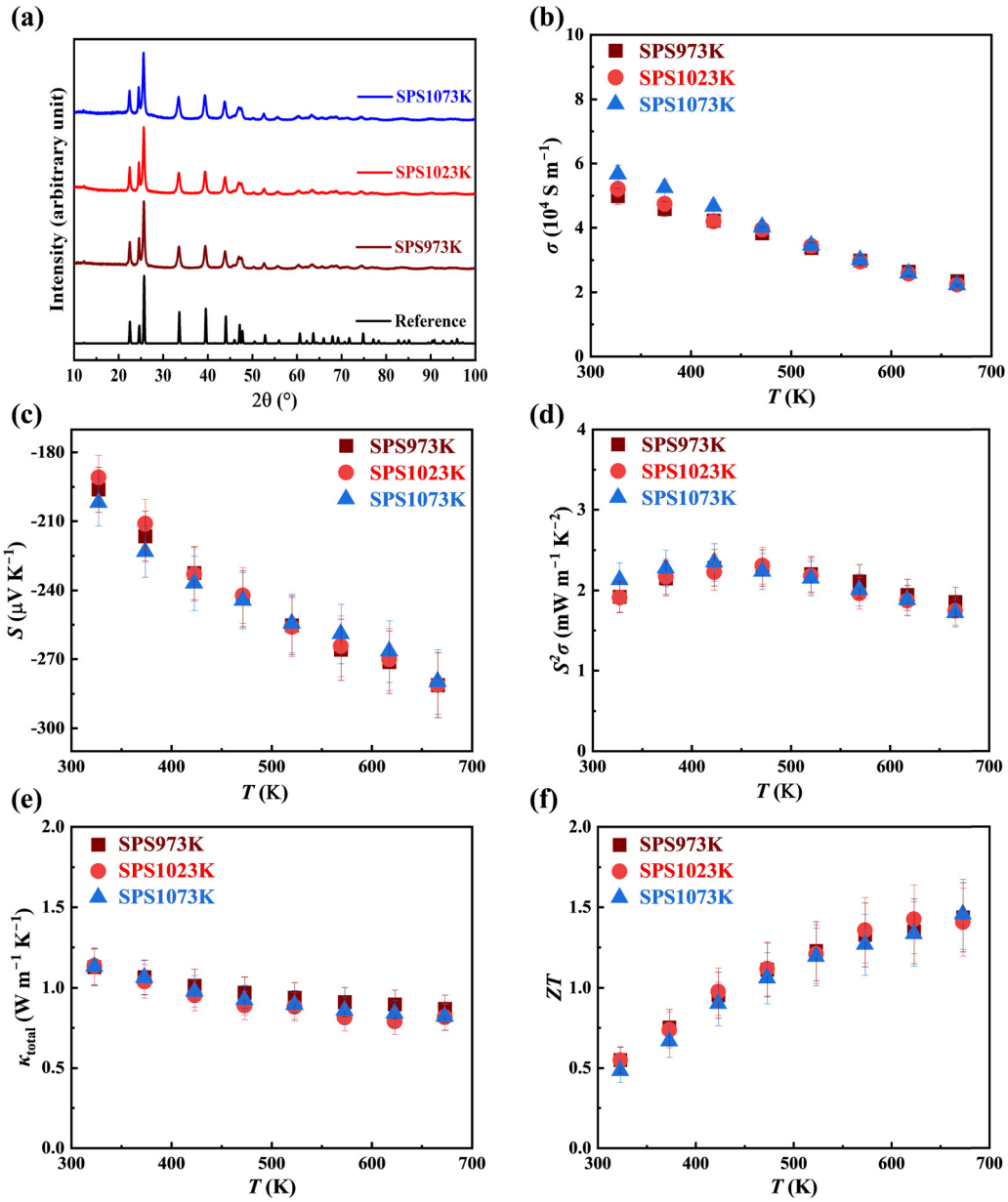

Fig. 1 (a) XRD of $Mg_3Sb_{1.5}Bi_{0.5}$ sintered at 973 K, 1023 K and 1073 K compared with the literature.[57] Thermoelectric properties of $Mg_3Sb_{1.5}Bi_{0.5}$ sintered at 973 K, 1023 K and 1073 K which includes (b) electrical conductivity (σ), (c) Seebeck coefficient (S), (d) power factor ($S^2\sigma$), (e) total thermal conductivity (κ_{total}) and (f) figure of merit (ZT).

1073 K. The σ values of all the samples decrease with increasing temperature, indicating a degenerate semiconducting behavior, which is consistent with a previous report.[57] The σ values vary from $\sim 5.2 \times 10^4$ S m^{-1} at 373 K to $\sim 2.6 \times 10^4$ S m^{-1} at 673 K in the whole temperature range and lie within the range of error bar for all the samples, confirming the minimal sintering temperature effect on σ. Similarly, very little sintering influence is observed for the Seebeck coefficient (S), ranging from -223 μV K^{-1} to -279 μV K^{-1} between 373 K and 673 K for all the pellets (Fig. 1c). However, at room temperature, there is a slight variation in the σ and S of $Mg_3Sb_{1.5}Bi_{0.5}$, which is attributed to the changes in the grain size with the sintering temperatures. These values are in good agreement with the previous report.[57] A maximum power factor ($S^2\sigma$) of ~ 2.2 mW m^{-1} K^{-2} at 423 K is obtained for all the samples (Fig. 1d). The total thermal conductivity (κ_{total}) of $Mg_3Sb_{1.5}Bi_{0.5}$ samples sintered at 973 K to 1073 K reduced from 1.13 W m^{-1} K^{-1} at room temperature to 0.81 W m^{-1} K^{-1} at 673 K (Fig. 1e). The maximum figure of merit (ZT) calculated was ~ 1.4 at 673 K, which is consistent with the previous report[57] ($ZT \sim 1.4$) for the same compound sintered at 973 K (Fig. 1f).

3.2. $SS_{p/f}/Mg_3Sb_{1.5}Bi_{0.5}/SS_{p/f}$ contacts

3.2.1. Specific contact resistivity. Our initial studies were carried out using stainless steel powder (SS_p) and were later changed to 0.5 mm thick foil (SS_f) due to its high density,

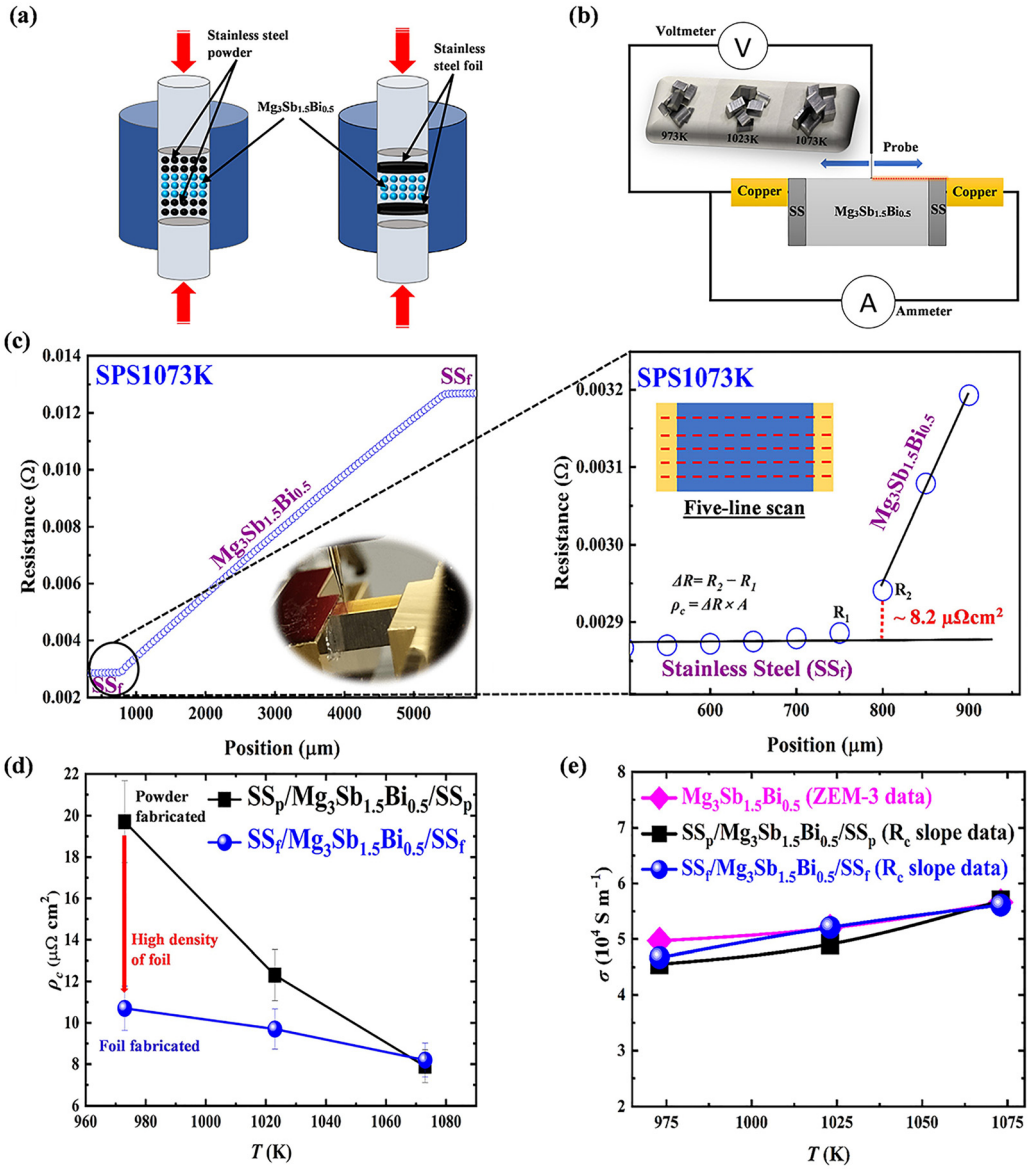

Fig. 2 (a) Schematic diagram of die preparation by using stainless steel 304 powder and foil. (b) Circuit diagram of resistance profiler. (c) Method to calculate the specific contact resistivity (ρ_c). (d) Specific contact resistivity (ρ_c) of powder and foil fabricated SS/$Mg_3Sb_{1.5}Bi_{0.5}$/SS sintered at 973 K, 1023 K and 1073 K. (e) Electrical conductivity (σ) comparison of powder/foil fabricated SS/$Mg_3Sb_{1.5}Bi_{0.5}$/SS by using resistance scan and $Mg_3Sb_{1.5}Bi_{0.5}$ by using a four probe method (ZEM-3 data).

process simplicity, and diffusion passivation characteristics (Fig. S1, ESI†). $Mg_3Sb_{1.5}Bi_{0.5}$ powders were sandwiched between $SS_{p/f}$ layers and sintered at temperatures between 973 K and 1073 K (Fig. 2a). All the TE disks ($SS_{p/f}/Mg_3Sb_{1.5}Bi_{0.5}/SS_{p/f}$) prepared at various sintering temperatures show good bonding and are crack-free without delamination after dicing. The specific contact resistivity (ρ_c) of the samples at three different sintering temperatures (973–1073 K) is measured using a resistance profiler with a circuit diagram shown in Fig. 2b. A sudden change in the slope at the $SS_f/Mg_3Sb_{1.5}Bi_{0.5}$ interface was characterized from the line scan as shown in Fig. 2c. The five-line scans are carried out at different sections of contacts and the arithmetic average is reported in Fig. 2d. It is observed that increasing the sintering temperature from 973 K to 1073 K results in lowering of the ρ_c from 19.7 μΩ cm^2 to 7.9 μΩ cm^2 for the $SS_p/Mg_3Sb_{1.5}Bi_{0.5}$ samples. The combined effect of improved sinter-bonding of SS_p particles and enhanced controlled diffusion helps to lower the ρ_c over ~60%. However, a significant diffusion between the TE materials and contact layers during the aging and long-term operation is a serious concern.[59,68] Thus, SS_p is replaced with SS_f, which results in the ρ_c of 10.7 μΩ cm^2 (~46% reduction compared to the SS_p sample) for the sample sintered at 973 K. High density of the foils (usually prepared by forging, rolling, and annealing) compared to sintered powders results in lower ρ_c for samples sintered even at 1023 K. However, with an increase in the sintering temperature to 1073 K, the ρ_c lowers to ~23% for $SS_f/Mg_3Sb_{1.5}Bi_{0.5}$ samples reaching ~8.2 μΩ cm^2. It is noteworthy that the σ calculated from the

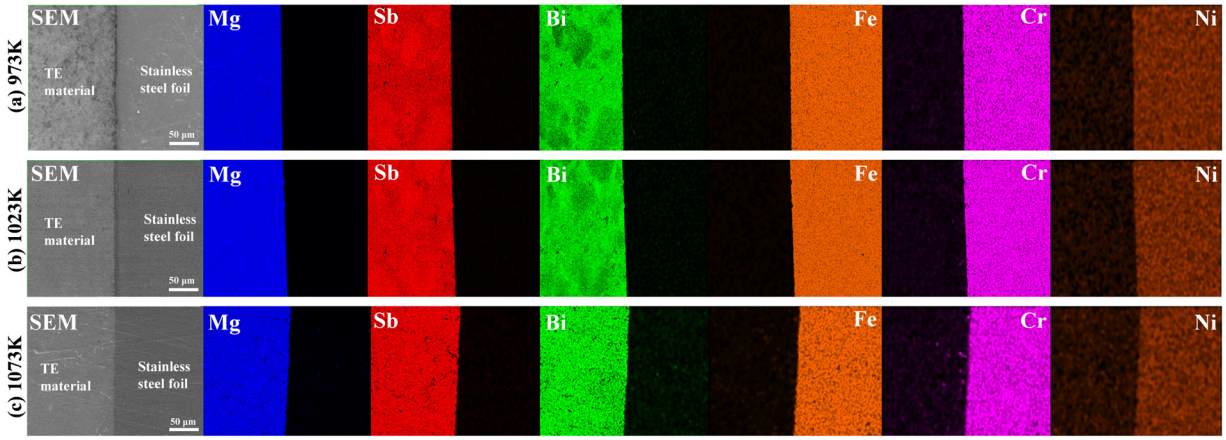

Fig. 3 SEM and EDX of $SS_f/Mg_3Sb_{1.5}Bi_{0.5}/SS_f$ sintered at (a) 973 K (b) 1023 K and (c) 1073 K.

slope of the resistance line scan on the $Mg_3Sb_{1.5}Bi_{0.5}$ for all samples (Fig. 2e and Tables S1, ESI†) is almost consistent with the σ measured by using the four-probe method (ZEM-3). This result further confirms the negligible influence of sintering temperature on the σ of TE material.

3.2.2. Microstructure. Fig. S2 (ESI†) shows the SEM+EDX mapping of stainless steel 304 powder (SS_p) contacts sintered between 973 K and 1073 K. Microstructure analysis reveals the diffusion of the elemental Sb and Bi into the SS_p contact layer ~100 μm for the $SS_p/Mg_3(Bi,Sb)_2/SS_p$ sample. Also, the SS_p region is porous, which results from the low densification of the powder form of stainless steel during the sintering. Qu *et al.* also reported the quick diffusion of Mg and Bi from the TE material to the non-dense Fe contact layers (>100 μm mixed layer) for Fe/Bi-rich $Mg_3(Bi,Sb)_2$.[59] The microstructure and EDX mapping of the foil fabricated $SS_f/Mg_3Sb_{1.5}Bi_{0.5}/SS_f$ contacts sintered at 973 K, 1023 K, and 1073 K are shown in Fig. 3. Similar microstructural features were observed at all sintering temperatures (973 K–1073 K), and the interfaces were crack-free and uniform. The samples sintered at 973 K and 1023 K show inhomogeneous distribution of Bi at the interfaces, which might result in off-stoichiometry in the chemical composition. However, the changes in the TE properties are minimal within the error limit (Fig. 1), while the 1073 K sintered sample shows homogeneous distribution of all the elements. Thus, we investigated the power generation characteristics and thermal stability of the 1073 K sintered sample. The sharp boundaries between SS_f and $Mg_3Sb_{1.5}Bi_{0.5}$ indicate the absence of notable atomic diffusion or reaction layer formation, indicating the effectiveness of SS_f as a suitable contact material for $Mg_3Sb_{1.5}Bi_{0.5}$. These results confirm that SS_f contact interface layers prevent diffusion, leading to uniform contacts without cracks or pores (Fig. S3–S5, ESI†).

The microstructural analysis and electrical contact resistivity reveal that the SS_f is promising as a contact interface layer sintered at 1073 K. Thus, we investigated the influence of the contact interface layer on the TE properties of the $Mg_3Sb_{1.5}Bi_{0.5}$ disk sintered at 1073 K by removing the SS_f contact layers (Fig. S6a, ESI†). Fig. S6(b)–(f) (ESI†) shows the comparison of temperature-dependent σ, S, $S^2\sigma$, κ_{total}, and ZT of the $Mg_3Sb_{1.5}Bi_{0.5}$ sample and $SS_f/Mg_3Sb_{1.5}Bi_{0.5}/SS_f$. Note that the TE properties were measured after removing the SS_f in the later sample. The TE properties of foil-removed $Mg_3Sb_{1.5}Bi_{0.5}$ are concurrent with the $Mg_3Sb_{1.5}Bi_{0.5}$ sample without foil as well as with the previous report[57] on the same compound.

3.2.3. Power generation characteristics of TE single leg $SS_f/Mg_3Sb_{1.5}Bi_{0.5}/SS_f$. Fig. 4 shows the power generation characteristics, including terminal voltage (V), electrical power output (P), output heat flow (Q_{out}) from the cold side, and conversion efficiency (η) of TE single leg $SS_f/Mg_3Sb_{1.5}Bi_{0.5}/SS_f$ as a function of electrical current (I). The hot-side temperature (T_h) of the TE leg varied between 323 K and 673 K, while the cold-side temperature was maintained at ~293–296 K. The open circuit voltage (V_{oc}), obtained from the intercept of V–I plot, increases from 4.8 mV at T_h = 323 K to 89 mV at T_h = 673 K (Fig. 4a). The internal resistance (R_{in}) is obtained by the slope of the V–I plot, which increases from 7.5 mΩ to 13.4 mΩ as T_h increases from 323 K to 673 K. This is attributed to the decrease of σ as the temperature increases (Fig. 1b). Maximum electrical output power (P_{max}) is obtained when the electronic load matches the internal resistance of the TE leg. The P_{max} increases from 0.7 mW at T_h = 323 K to 146 mW at T_h = 673 K (Fig. 4b). The open circuit heat flow (Q_{oc}) obtained from the intercept of the Q_{out}–I plot, which increases from 195.9 mW at 323 K to 1960 mW at 673 K. Fig. 4c shows that the Q_{out} increases with I at every rise in ΔT due to Peltier heat and Joule heat, which are proportional to I and I^2, respectively.[76] At T_h = 323 K, the maximum conversion efficiency (η_{max}) of ~0.46% is obtained, which reaches ~9.3% as the T_h rises to 673 K (Fig. 4d). This result is comparable with the previously reported η_{max} of the single-leg TE $Mg_3(Sb,Bi)_2$ with SS304 powder used as contact interface layers.[68] The η_{max} of ~9.3% obtained in this study is also comparable to the efficiencies of single-leg TE $Mg_3(Sb,Bi)_2$ with other contact interface layers[51,52,55,60,62,66,74,77–79] (Fig. 4e). However, long-term thermal stability analyses of these high efficiencies are still lacking in previous studies.

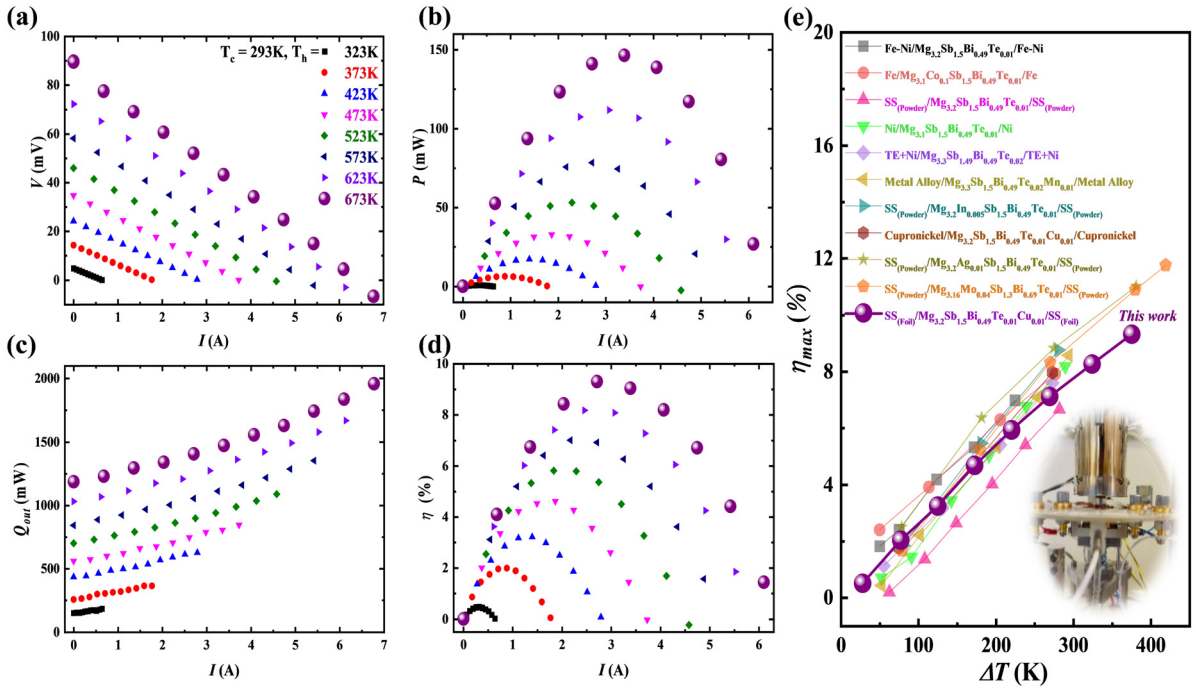

Fig. 4 Power generation characteristics of $SS_f/Mg_3Sb_{1.5}Bi_{0.5}/SS_f$ sintered at 1073 K, which includes (a) terminal voltage (V), (b) power output (P), (c) output heat flow (Q_{out}) at cold side, (d) conversion efficiency (η) at different T_h, (e) maximum conversion efficiency (η_{max}) compared with the reported literature.[51,52,55,60,62,64,66,74,77–79]

3.3. Thermal stability evaluation of $SS_f/Mg_3Sb_{1.5}Bi_{0.5}/SS_f$

The thermal stability of $SS_f/Mg_3Sb_{1.5}Bi_{0.5}/SS_f$ was systematically evaluated by performing an aging test at 673 K over 7, 15, and 30 days and the corresponding microstructural investigation. The microstructural analysis showed a stable, crack-free contact interface, with no evidence of element diffusion after aging for 30 days (Fig. S7–S9, ESI†). Moreover, the stability of the interface was evaluated by measuring the specific contact resistivity (ρ_c) of the $SS_f/Mg_3Sb_{1.5}Bi_{0.5}/SS_f$ aged at 673 K for 0, 7, 15, and 30 days (Fig. S10, ESI†). The specific contact resistivity (ρ_c) was ~8.2 μΩ cm^2 and showed variations during the thermal aging at 673 K. Initially, the specific contact resistivity (ρ_c) decreased from ~8.2 μΩ cm^2 to ~6 μΩ cm^2 after 7 days' aging. This trend is similar to the previous report of Fe foil and Bi-rich $Mg_3(Sb,Bi)_2$, due to the formation of a thin intermediate layer after 3 days of aging at 573 K.[59] However, we did not observe any intermediate layer of SS foil and Sb-rich $Mg_3(Sb,Bi)_2$ within the detection limit of SEM. The initial decrease in specific contact resistivity (ρ_c) might be due to the chemical reaction with nano intermediate layer formation. The volatile Mg loss at the interfaces may cause a change in the chemical composition,[61] which could result in slight changes in the carrier concentration and further rise in specific contact resistivity (ρ_c) up to ~14.8 μΩ cm^2 after 30 days' aging (Fig. 5a). It is noteworthy that the aging test performed in this study is at a higher temperature (673 K) for a long time (30 days) as compared to the previous reports[48,59,71,74,75,77] on the $Mg_3(Sb,Bi)_2$-based TE legs. For example, the ρ_c increased from ~5.6 μΩ cm^2 to ~11 μΩ cm^2 for the $Mg_{3.2}Sb_{1.5}Bi_{0.49}Te_{0.01}$/SS powder after performing an aging test at a lower temperature (523 K) and for a smaller period (200 hours, *i.e.*, 9 days).[68] Furthermore, the power generation characteristics of the $SS_f/Mg_3Sb_{1.5}Bi_{0.5}/SS_f$ were also evaluated after aging at 673 K for 7, 15, and 30 days (Fig. S11, ESI†). No significant variation in the internal resistance (R_{in}) of TE single leg $SS_f/Mg_3Sb_{1.5}Bi_{0.5}/SS_f$ is observed after aging of 30 days. The R_{in} slightly increased from 13.4 mΩ to 14.2 mΩ after 30 days of aging (Fig. 5b). Moreover, no influence of aging on the V_{oc} indicates the good chemical and thermal stability of the $SS_f/Mg_3Sb_{1.5}Bi_{0.5}/SS_f$. The maximum power density ($P_{d(max)}$ ~1.7 W cm^{-2}) shows minimal variation after 30 days of annealing at 673 K (Fig. 5c). The maximum conversion efficiency (η_{max}) of the single leg drops slightly from 9.3% to 8.9% after 30 days of annealing at 673 K, indicating the good thermal stability (Fig. 5d). Additionally, the TE properties of $SS_f/Mg_3Sb_{1.5}Bi_{0.5}/SS_f$ are consistent before and after aging of 30 days (Fig. S12, ESI†). Overall, the negligible influence on the TE properties, microstructure, specific contact resistivity (ρ_c), power generation characteristics of the $SS_f/Mg_3Sb_{1.5}Bi_{0.5}/SS_f$ are observed, confirming the excellent stability of material and contact interface layer at high temperatures (Fig. S13, ESI†), making it a promising candidate for long term thermoelectric device applications.

4. Conclusions

In this work, we demonstrated the influence of sintering conditions on the optimization of contact layers for the $Mg_3Sb_{1.5}Bi_{0.5}$. At a higher sintering temperature (1073 K), the contact between the SS and $Mg_3Sb_{1.5}Bi_{0.5}$ is improved due to the increased

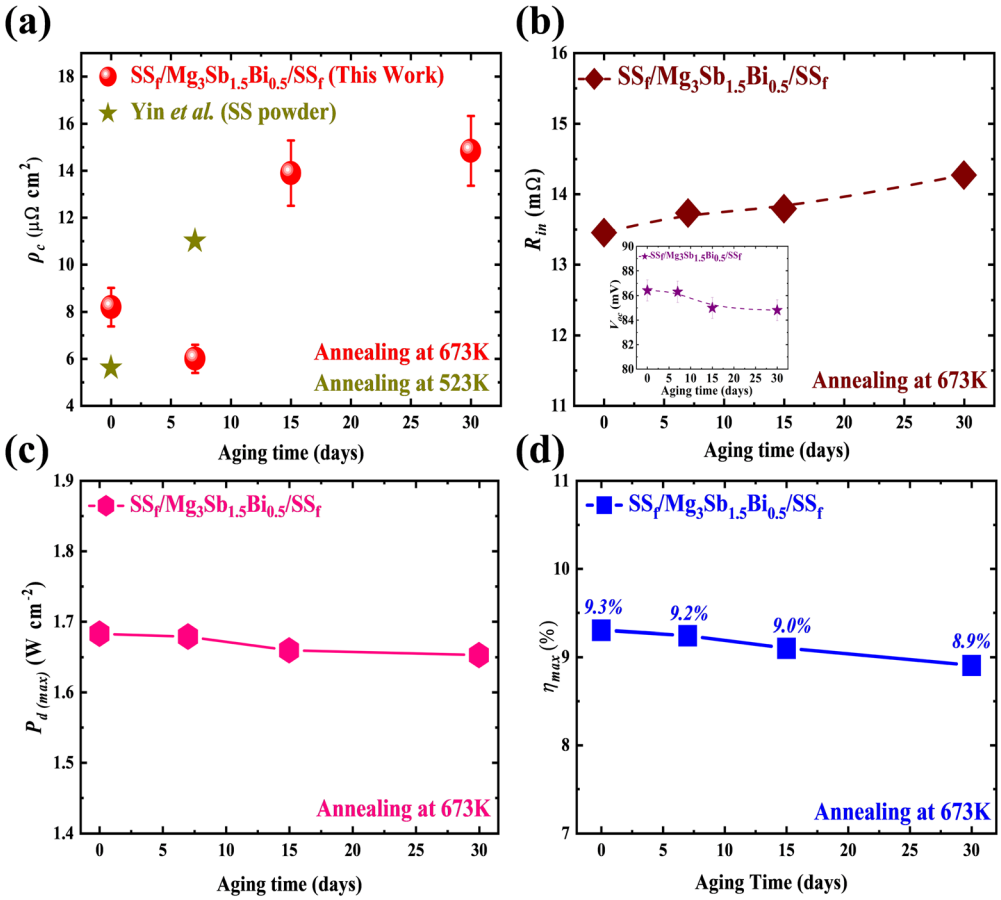

Fig. 5 Power generation characteristics of $SS_f/Mg_3Sb_{1.5}Bi_{0.5}/SS_f$ with aging of 7, 15 and 30 days, which includes (a) Specific contact resistivity (ρ_c) with the reported literature.[68] (b) Internat resistance (R_{in}) (c) Maximum power density ($P_{d(max)}$). (d) Maximum conversion efficiency (η_{max}).

adhesive strength and results in a significant reduction (~60%) in the specific contact resistivity (ρ_c) at their interface. A uniform, crack-free interface with low ρ_c led to a maximum conversion efficiency (η_{max}) of 9.3% at a temperature difference (ΔT) of 380 K for $SS_f/Mg_3Sb_{1.5}Bi_{0.5}/SS_f$ TE single leg sintered at 1073 K. Moreover, our work reveals that the $Mg_3Sb_{1.5}Bi_{0.5}$-based TE single leg shows the good thermal stability without much degradation in the TE properties and power generation characteristics after aging at 673 K for 30 days. This work facilitates the advancement in contact layer optimization through process engineering for the $Mg_3(Sb,Bi)_2$-based compounds.

Data availability

Data will be made available upon reasonable request to the corresponding author.

Conflicts of interest

The authors declare that they have no competing financial interests or personal relationships that could have appeared to influence the work reported in this paper.

Acknowledgements

This work was supported by the JST Mirai Program grant number JPMJMI19A1. We also acknowledge the support of the MEXT fellowship to M. F. A. Institutional support from the JSPS WPI Academy Program is also acknowledged.

References

1 T. Mori and S. Priya, *MRS Bull.*, 2018, **43**, 176–180.
2 L. E. Bell, *Science*, 2008, **321**, 1457–1461.
3 D. Champier, *Energy Convers. Manage.*, 2017, **140**, 167–181.
4 F. J. DiSalvo, *Science*, 1999, **285**, 703–706.
5 I. Petsagkourakis, K. Tybrandt, X. Crispin, I. Ohkubo, N. Satoh and T. Mori, *Sci. Technol. Adv. Mater.*, 2018, **19**, 836–862.
6 R. O'Brien, R. Ambrosi, N. Bannister, S. Howe and H. V. Atkinson, *J. Nucl. Mater.*, 2008, **377**, 506–521.
7 T. Hendricks, T. Caillat and T. Mori, *Energies*, 2022, **15**, 7307.
8 Q. H. Zhang, X. Y. Huang, S. Q. Bai, X. Shi, C. Uher and L. D. Chen, *Adv. Eng. Mater.*, 2016, **18**, 194–213.
9 D. Rowe and G. Min, *J. Power Sources*, 1998, **73**, 193–198.
10 G. Tan, M. Ohta and M. G. Kanatzidis, *Philos. Trans. R. Soc., A*, 2019, **377**, 20180450.

11 G. J. Snyder and T. S. Ursell, *Phys. Rev. Lett.*, 2003, **91**, 148301.
12 A. F. Ioffe, L. Stil'Bans, E. Iordanishvili, T. Stavitskaya, A. Gelbtuch and G. Vineyard, *Phys. Today*, 1959, **12**, 42.
13 X.-L. Shi, J. Zou and Z.-G. Chen, *Chem. Rev.*, 2020, **120**, 7399–7515.
14 N. M. Yatim, N. Z. I. M. Sallehin, S. Suhaimi and M. A. Hashim, *AIP Conference Proceedings*, AIP Publishing, 2018.
15 B. Poudel, Q. Hao, Y. Ma, Y. Lan, A. Minnich, B. Yu, X. Yan, D. Wang, A. Muto and D. Vashaee, *Science*, 2008, **320**, 634–638.
16 J. Wei, L. Yang, Z. Ma, P. Song, M. Zhang, J. Ma, F. Yang and X. Wang, *J. Mater. Sci.*, 2020, **55**, 12642–12704.
17 J. Pei, B. Cai, H.-L. Zhuang and J.-F. Li, *Natl. Sci. Rev.*, 2020, **7**, 1856–1858.
18 Q. Han, P.-A. Zong, H. Liu, Z. Zhang, K. Shen, M. Liu, Z. Mao, Q. Song and S. Bai, *ACS Appl. Mater. Interfaces*, 2024, **8**(5), 27541–27549.
19 H. Li, J. Feng, L. Zhao, E. Min, H. Zhang, A. Li, J. Li and R. Liu, *ACS Appl. Mater. Interfaces*, 2024, **16**, 22147–22154.
20 J. D'angelo, E. D. Case, N. Matchanov, C.-I. Wu, T. P. Hogan, J. Barnard, C. Cauchy, T. Hendricks and M. G. Kanatzidis, *J. Electron. Mater.*, 2011, **40**, 2051–2062.
21 K. Biswas, J. He, I. D. Blum, C.-I. Wu, T. P. Hogan, D. N. Seidman, V. P. Dravid and M. G. Kanatzidis, *Nature*, 2012, **489**, 414–418.
22 X. Hu, P. Jood, M. Ohta, M. Kunii, K. Nagase, H. Nishiate, M. G. Kanatzidis and A. Yamamoto, *Energy Environ. Sci.*, 2016, **9**, 517–529.
23 T. Fu, X. Yue, H. Wu, C. Fu, T. Zhu, X. Liu, L. Hu, P. Ying, J. He and X. Zhao, *J. Materiomics*, 2016, **2**, 141–149.
24 Y. Xiao and L.-D. Zhao, *npj Quantum Mater.*, 2018, **3**, 55.
25 P. Jood, M. Ohta, A. Yamamoto and M. G. Kanatzidis, *Joule*, 2018, **2**, 1339–1355.
26 P. Sauerschnig, N. Saitou, M. Koshino, T. Ishida, A. Yamamoto and M. Ohta, *ACS Appl. Mater. Interfaces*, 2024, **16**, 46421–46432.
27 M. Darwiche, J. Faraj, K. Chahine, A. Shaito, S. Awad, M. Mortazavi and M. Khaled, *Results Eng.*, 2024, 103354.
28 A. Samarelli, L. F. Llin, S. Cecchi, J. Frigerio, D. Chrastina, G. Isella, E. M. Gubler, T. Etzelstorfer, J. Stangl and Y. Zhang, *Solid-State Electron.*, 2014, **98**, 70–74.
29 A. Nozariasbmarz, A. Agarwal, Z. A. Coutant, M. J. Hall, J. Liu, R. Liu, A. Malhotra, P. Norouzzadeh, M. C. Oeztuerk and V. P. Ramesh, *Jpn. J. Appl. Phys.*, 2017, **56**, 05DA04.
30 R. Dhawan, P. Madusanka, G. Hu, J. Debord, T. Tran, K. Maggio, H. Edwards and M. Lee, *Nat. Commun.*, 2020, **11**, 4362.
31 S. Fujimoto, K. Nagase, H. Ohshima, M. Murata, A. Yamamoto and C. H. Lee, *Adv. Eng. Mater.*, 2022, **24**, 2101520.
32 G. Rogl, A. Grytsiv, P. Rogl, E. Bauer and M. Zehetbauer, *Intermetallics*, 2011, **19**, 546–555.
33 G. Rogl, A. Grytsiv, P. Rogl, N. Peranio, E. Bauer, M. Zehetbauer and O. Eibl, *Acta Mater.*, 2014, **63**, 30–43.
34 J. R. Salvador, J. Y. Cho, Z. Ye, J. E. Moczygemba, A. J. Thompson, J. W. Sharp, J. D. Koenig, R. Maloney, T. Thompson and J. Sakamoto, *Phys. Chem. Chem. Phys.*, 2014, **16**, 12510–12520.
35 A. U. Khan, K. Kobayashi, D.-M. Tang, Y. Yamauchi, K. Hasegawa, M. Mitome, Y. Xue, B. Jiang, K. Tsuchiya and D. Golberg, *Nano Energy*, 2017, **31**, 152–159.
36 P.-a Zong, R. Hanus, M. Dylla, Y. Tang, J. Liao, Q. Zhang, G. J. Snyder and L. Chen, *Energy Environ. Sci.*, 2017, **10**, 183–191.
37 G. Nie, S. Suzuki, T. Tomida, A. Sumiyoshi, T. Ochi, K. Mukaiyama, M. Kikuchi, J. Guo, A. Yamamoto and H. Obara, *J. Electron. Mater.*, 2017, **46**, 2640–2644.
38 S. El Oualid, I. Kogut, M. Benyahia, E. Geczi, U. Kruck, F. Kosior, P. Masschelein, C. Candolfi, A. Dauscher and J. D. Koenig, *Adv. Energy Mater.*, 2021, **11**, 2100580.
39 S. Chen and Z. Ren, *Mater. Today*, 2013, **16**, 387–395.
40 C. Fu, S. Bai, Y. Liu, Y. Tang, L. Chen, X. Zhao and T. Zhu, *Nat. Commun.*, 2015, **6**, 8144.
41 J. Yu, Y. Xing, C. Hu, Z. Huang, Q. Qiu, C. Wang, K. Xia, Z. Wang, S. Bai and X. Zhao, *Adv. Energy Mater.*, 2020, **10**, 2000888.
42 W. Li, S. Ghosh, N. Liu and B. Poudel, *Joule*, 2024, **8**(5), 1274–1311.
43 R. Chen, H. Kang, R. Min, Z. Chen, E. Guo, X. Yang and T. Wang, *Int. Mater. Rev.*, 2024, **69**, 83–106.
44 D. M. Rowe, *CRC handbook of thermoelectrics*, CRC Press, 2018.
45 J. Mao, Z. Liu, J. Zhou, H. Zhu, Q. Zhang, G. Chen and Z. Ren, *Adv. Phys.*, 2018, **67**, 69–147.
46 R. He, G. Schierning and K. Nielsch, *Adv. Mater. Technol.*, 2018, **3**, 1700256.
47 K. Xiong, W. Wang, H. N. Alshareef, R. P. Gupta, J. B. White, B. E. Gnade and K. Cho, *J. Phys. D: Appl. Phys.*, 2010, **43**, 115303.
48 X. Wu, Z. Han, Y. Zhu, B. Deng, K. Zhu, C. Liu, F. Jiang and W. Liu, *Acta Mater.*, 2022, **226**, 117616.
49 T. Kanno, H. Tamaki, H. K. Sato, S. D. Kang, S. Ohno, K. Imasato, J. J. Kuo, G. J. Snyder and Y. Miyazaki, *Appl. Phys. Lett.*, 2018, **112**, 033903.
50 J. Mao, H. Zhu, Z. Ding, Z. Liu, G. A. Gamage, G. Chen and Z. Ren, *Science*, 2019, **365**, 495–498.
51 H. Shang, Z. Liang, C. Xu, S. Song, D. Huang, H. Gu, J. Mao, Z. Ren and F. Ding, *Acta Mater.*, 2020, **201**, 572–579.
52 L. Wang, N. Sato, Y. Peng, R. Chetty, N. Kawamoto, D. H. Nguyen and T. Mori, *Adv. Energy Mater.*, 2023, **13**, 2301667.
53 Z. Liang, C. Xu, S. Song, X. Shi, W. Ren and Z. Ren, *Adv. Funct. Mater.*, 2023, **33**, 2210016.
54 H. Cho, S. Y. Back, N. Sato, Z. Liu, W. Gao, L. Wang, H. D. Nguyen, N. Kawamoto and T. Mori, *Adv. Funct. Mater.*, 2024, **34**, 2407017.
55 L. Wang, W. Zhang, S. Y. Back, N. Kawamoto, D. H. Nguyen and T. Mori, *Nat. Commun.*, 2024, **15**, 6800.
56 S. Bano, R. Chetty, J. Babu and T. Mori, *Device*, 2024, **2**, 100408.
57 Z. Liu, N. Sato, W. Gao, K. Yubuta, N. Kawamoto, M. Mitome, K. Kurashima, Y. Owada, K. Nagase and C.-H. Lee, *Joule*, 2021, **5**, 1196–1208.
58 Z. Liu, W. Gao, H. Oshima, K. Nagase, C.-H. Lee and T. Mori, *Nat. Commun.*, 2022, **13**, 1120.
59 N. Qu, Y. Sun, Z. Liu, L. Xie, Y. Zhu, H. Wu, R. Chai, J. Cheng, F. Guo and Q. Zhang, *Adv. Energy Mater.*, 2024, **14**, 2302818.
60 R. Chetty, J. Babu and T. Mori, *ACS Appl. Energy Mater.*, 2024, **7**(24), 12112–12118.

61 Y. Fu, X. Ai, Z. Hu, S. Zhao, X. Lu, J. Huang, A. Huang, L. Wang, Q. Zhang and W. Jiang, *Nat. Commun.*, 2024, **15**, 9355.
62 C. Xu, Z. Liang, H. Shang, D. Wang, H. Wang, F. Ding, J. Mao and Z. Ren, *Mater. Today Phys.*, 2021, **17**, 100336.
63 Y. Fu, Q. Zhang, Z. Hu, M. Jiang, A. Huang, X. Ai, S. Wan, H. Reith, L. Wang and K. Nielsch, *Energy Environ. Sci.*, 2022, **15**, 3265–3274.
64 P. Ying, R. He, J. Mao, Q. Zhang, H. Reith, J. Sui, Z. Ren, K. Nielsch and G. Schierning, *Nat. Commun.*, 2021, **12**, 1121.
65 Z. Bu, X. Zhang, Y. Hu, Z. Chen, S. Lin, W. Li, C. Xiao and Y. Pei, *Nat. Commun.*, 2022, **13**, 237.
66 Q. Zhu, S. Song, H. Zhu and Z. Ren, *J. Power Sources*, 2019, **414**, 393–400.
67 Z. Liang, C. Xu, H. Shang, Q. Zhu, F. Ding, J. Mao and Z. Ren, *Mater. Today Phys.*, 2021, **19**, 100413.
68 L. Yin, C. Chen, F. Zhang, X. Li, F. Bai, Z. Zhang, X. Wang, J. Mao, F. Cao and X. Chen, *Acta Mater.*, 2020, **198**, 25–34.
69 Z. Bu, X. Zhang, Y. Hu, Z. Chen, S. Lin, W. Li and Y. Pei, *Energy Environ. Sci.*, 2021, **14**, 6506–6513.
70 Y. Liu, Y. Geng, Y. Dou, X. Wu, L. Hu, F. Liu, W. Ao and C. Zhang, *Small*, 2023, **19**, 2303840.
71 Y. Wang, J. Chen, Y. Jiang, M. Ferhat, S. Ohno, Z. A. Munir, W. Fan and S. Chen, *ACS Appl. Mater. Interfaces*, 2022, **14**, 33419–33428.
72 L. Yin, X. Li, X. Bao, J. Cheng, C. Chen, Z. Zhang, X. Liu, F. Cao, J. Mao and Q. Zhang, *Nat. Commun.*, 2024, **15**, 1468.
73 X. Wu, J. Huang, Z. Zhou, Z. Han, F. Jiang, H. Li, Y. Wang, K. Zhu and W. Liu, *Mater. Lab*, 2012, **24**(11), 1418–1423.
74 X. Wu, Y. Lin, Z. Han, H. Li, C. Liu, Y. Wang, P. Zhang, K. Zhu, F. Jiang and J. Huang, *Adv. Energy Mater.*, 2022, **12**, 2203039.
75 J. Yang, G. Li, H. Zhu, N. Chen, T. Lu, J. Gao, L. Guo, J. Xiang, P. Sun and Y. Yao, *Joule*, 2022, **6**, 193–204.
76 R. Chetty, J. Babu and T. Mori, *Joule*, 2024, **8**, 556–562.
77 S. Song, Z. Liang, C. Xu, Y. Wang, X. Shi, W. Ren and Z. Ren, *Soft Sci.*, 2022, **2**, 13.
78 N. Kumari, A. Singh and T. Dasgupta, *ACS Appl. Electron. Mater.*, 2023, **6**, 2935–2941.
79 J. Li, R. Chetty, Z. Liu, W. Gao and T. Mori, *Small*, 2024, **21**(2), 2408059.